

Ultrasound Pulse-Echo Imaging with an Optimized Propagator

Lianjie Huang

Los Alamos National Laboratory, MS D443
Los Alamos, NM 87545, USA
ljh@lanl.gov

Cuiping Li and Neb Duric

Karmanos Cancer Institute
4100 John R. Street, Detroit, MI 48201, USA
lic@karmanos.org; duric@karmanos.org

Youli Quan

Stanford University, Department of Geophysics
Stanford, CA 94305, USA
quany@stanford.edu

Kenneth M. Hanson

Los Alamos National Laboratory, MS B283
Los Alamos, NM 87545, USA
kmh@lanl.gov

Abstract

Properly accounting for ultrasound scattering from heterogeneities within the breast is essential for high-resolution ultrasound breast imaging. This requires a reflectivity image reconstruction method capable of accurately handling ultrasound scattering. We develop an optimized ultrasound-wave propagator for reflectivity image reconstruction using pulse-echo ultrasound signals. The method is based on a solution of one-way wave equation and recursive inward continuation of ultrasound wavefields in the frequency-space and frequency-wavenumber domains using a heterogeneous sound-speed model of the breast obtained from tomography. It minimizes ultrasound phase errors during wavefield inward continuation while maintaining the advantage of high computational efficiency. Pulse-echo ultrasound imaging tests for a numerical breast phantom demonstrate that our optimized method has the potential to improve the reliability and accuracy of ultrasound breast imaging.

1. Introduction

Ultrasonography uses pulse-echo ultrasound for imaging and is a common modality for breast cancer diagnosis. In addition, ultrasound breast imaging is one of the most promising screening tools as an alternative to x-ray mammography [9]. The primary limitation of ultrasonography is that ultrasound images contain a great deal of image noises. This limitation is mainly caused by ultrasound scattering from breast heterogeneities. Sound speeds and densities of breast tissue are inhomogeneous, and those of tumors are different from the surrounding tissues. These differences in mechanical properties result in ultrasound scattering, partic-

ularly in dense breasts. With the development of new circular ultrasound arrays for clinical breast imaging [6, 2, 10, 1], heterogeneous sound-speed models of the breast can be accurately obtained using ultrasound tomography [5, 7, 8]. Reflectivity image reconstruction can be significantly improved by using the heterogeneous sound-speed models for imaging. The split-step Fourier propagator was recently used for ultrasound pulse-echo imaging to approximately account for ultrasound scattering [4]. The method is computationally much more efficient than that based on finite-difference time-domain wave-equation method [3].

In this paper, we develop an optimized ultrasound-wave propagator for ultrasound reflectivity image reconstruction using a solution of one-way wave equation in heterogeneous media. It is optimized for the sound-speed perturbation range of the breast to minimize ultrasound phase errors during wavefield inward continuation. The method performs one additional step of ultrasound scattering compensation during each recursive step of inward continuation of ultrasound wavefields, in addition to the split-step Fourier implementation. It significantly improves imaging accuracy compared to the split-step Fourier method while it is still much more computationally efficient than the finite-difference-based imaging method. We use synthetic ultrasound pulse-echo data for a numerical breast phantom to demonstrate the improved imaging capability of our optimized imaging method.

2. Optimized propagator

Ultrasound wave propagation in the breast is governed by the acoustic-wave equation, which can be decomposed into two one-way wave equations describing wave propagation in opposite directions. One of these one-way wave

equations in the frequency-space domain is given by

$$\frac{\partial U(x, z; \omega)}{\partial z} = -i Q(x, z; \omega) U(x, z; \omega), \quad (1)$$

where U is the pressure and the operator Q is defined by

$$Q \equiv \sqrt{\frac{\omega^2}{c^2(x, z)} + \frac{\partial^2}{\partial x^2}} = \frac{\omega}{c(x, z)} R, \quad (2)$$

where ω is the circular frequency, (x, z) is the space location, c is the sound speed, and R is the square-root operator given by

$$R \equiv \sqrt{1 - X^2}, \quad (3)$$

with

$$X^2 \equiv -\frac{c^2}{\omega^2} \frac{\partial^2}{\partial x^2}. \quad (4)$$

The formal solution of eq. (1) is

$$U(x, z + \Delta z; \omega) = \exp \left\{ -i \int Q dz \right\} U(x, z; \omega), \quad (5)$$

which extrapolates the ultrasound wavefield U from the depth level at z to the next depth level at $z + \Delta z$.

We expand the square-root operator R in the form

$$R \approx 1 - \frac{a X^2}{1 - b X^2}, \quad (6)$$

where a and b are free coefficients. The difference between operator Q , given by eq. (2) and that in a background medium with a sound speed of $c_0(z)$ is

$$D = \frac{\omega}{c} \sqrt{1 - X^2} - \frac{\omega}{c_0} \sqrt{1 - X_0^2} \quad (7)$$

where X_0^2 is given by

$$X_0^2 = -\frac{c_0^2}{\omega^2} \frac{\partial^2}{\partial x^2} = \frac{X^2}{m^2} \quad (8)$$

where the sound-speed contrast $m(x, z) = c(x, z)/c_0(z)$ is the reciprocal of the refraction index. Making use of eq. (6), eq. (7) can be approximated as

$$D \approx \left(\frac{\omega}{c} - \frac{\omega}{c_0} \right) - \frac{\omega}{c_0} \frac{a(m-1)X_0^2}{1 - b(1+m^2)X_0^2}. \quad (9)$$

Therefore, eq. (2) can be approximated by

$$Q \approx \sqrt{\frac{\omega^2}{c_0^2} + \frac{\partial^2}{\partial x^2}} + \frac{\omega}{c_0} \left(\frac{1}{m} - 1 \right) - \frac{\omega}{c_0} \frac{a(m-1)X_0^2}{1 - b(1+m^2)X_0^2}. \quad (10)$$

The formal solution (5) with the the first two terms of eq. (10) is the split-step Fourier operator [4]. The formal

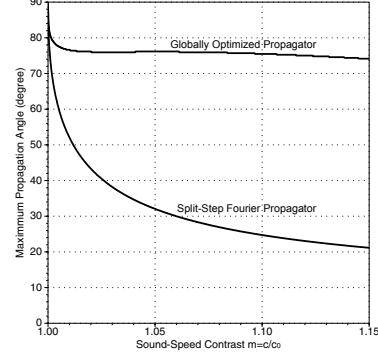


Figure 1: The relationships of the maximum propagation angle within 1% of phase error versus the sound-speed contrast for the optimized propagator and the split-step Fourier propagator.

solution (5) with the third term of eq. (10) is implemented using an implicit finite-difference scheme.

The phase error is zero along the primary inward continuation direction. Then it increases with increasing the propagation angle relative to the primary direction. We substitute eq. (10) into eq. (5), and minimize the phase error for the entire sound-speed perturbation range of the breast to obtain the optimized values of coefficients a and b . The resulting propagator is termed the globally optimized Fourier finite-difference propagator.

Assuming the maximum sound-speed perturbation within the breast is 15%, Fig. 1 depicts the relationships of the maximum propagation angle within 1% of phase error versus the sound-speed contrast for the optimized propagator and the split-step Fourier propagator. It shows that the optimized propagator can accurately handle much large propagation angles than the split-step Fourier propagator, that is, it is much more accurate for large propagation angles compared with the split-step Fourier propagator.

3. Numerical pulse-echo imaging examples

We use a numerical breast phantom shown in Fig. 2 to study the pulse-echo imaging capability of our optimized propagator. The phantom is derived from *in vivo* breast tomography, and the region with high sound-speed is a tumor. An ultrasound pulse with the second derivative of a Gaussian time function and a central frequency of 1 MHz is emitted from each transducer along the white solid circle, and ultrasound pulse-echo signals are recorded by the same transducer. Numerical data are generated using a finite-difference time-domain acoustic-wave equation in heterogeneous media.

Figure 3 shows different sound-speed transmission to-

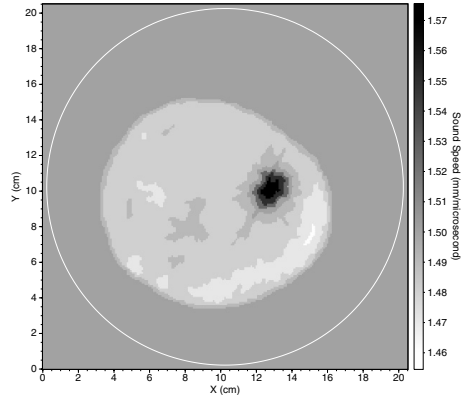


Figure 2: Numerical breast phantom derived from sound-speed transmission tomography of an *in vivo* breast dataset. The white solid circle indicates the locations of transducers.

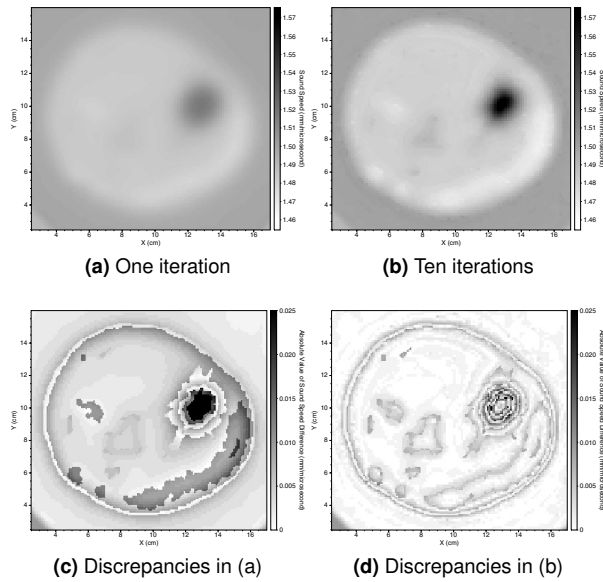
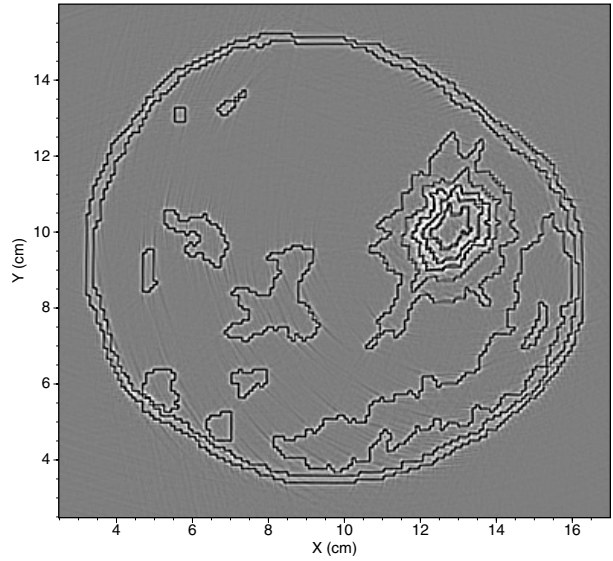
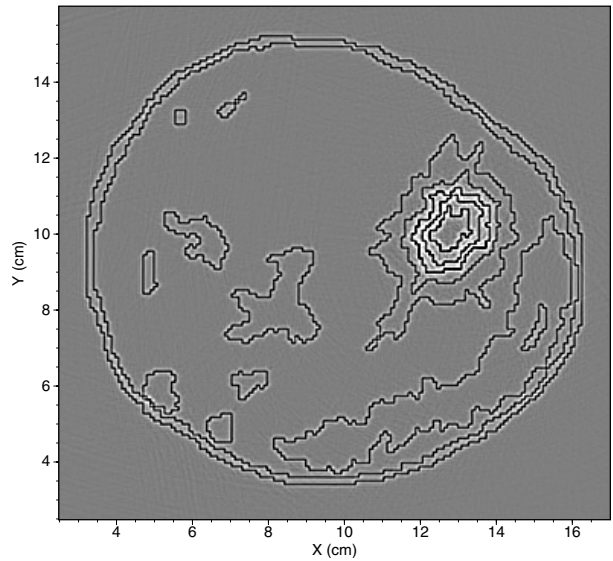


Figure 3: Sound-speed transmission tomography results of the numerical breast phantom with one iteration (a) and ten iterations (b), together with their absolute values of sound-speed discrepancies (c-d).

mography results (a)-(b) of the numerical breast phantom, together with their absolute values of sound-speed discrepancies (c)-(d), that is, the absolute values of the differences between Figs. (a)-(b) and the correct sound speed in Fig. 2. The discrepancies/errors of the tomography result with ten iterations are considerably smaller than that with one iteration. In addition, the largest discrepancies occur in the tumor region, as shown in Figs. 3(c) and (d).



(a) Reflectivity image reconstructed using Fig. 3(a)



(b) Reflectivity image reconstructed with Fig. 3(b)

Figure 4: Reflectivity images reconstructed using the optimized propagator and heterogeneous sound-speed tomography results in Fig. 3.

Figure 4 displays reflectivity images of the numerical phantom reconstructed using the optimized propagator and the heterogeneous sound-speed models in Fig. 3(a) and (b). Fig. 4(a) contains significant more image noises than Fig. 4(b). In addition, the images in the tumor region in Fig. 4(a) are not well reconstructed, while those in Fig. 4(b) are well imaged. Fig. 4(a) demonstrates that large sound-speed discrepancies as shown in Fig. 3(c) can result in sig-

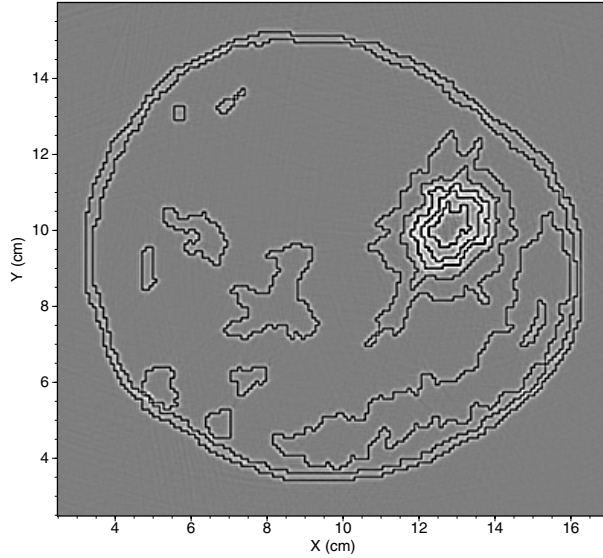


Figure 5: Reflectivity images reconstructed using the optimized propagator and the correct sound speed of the breast phantom in Fig. 2.

nificant image artifacts in reflectivity images, because ultrasound scattering is not properly accounted for during reflectivity image reconstruction.

We investigate reflectivity image artifacts caused by the propagator inaccuracy and the sound-speed discrepancy. High-resolution and high-quality ultrasound images can be obtained by properly accounting for ultrasound scattering during reflectivity image reconstruction. This requires an accurate wave propagator and an accurate sound-speed model. Reflectivity image artifacts (including image noise, incorrect image location and amplitudes) are caused not only by the propagator inaccuracy, but also by the discrepancies/errors in the sound-speed model used for image reconstruction. Low ultrasound data quality and improper transducer distribution can also contribute to image artifacts. We do not include these factors in this study.

Figure 5 is a reflectivity image reconstructed using the optimized and the correct sound-speed of the numerical breast phantom in Fig. 2. It does not contain any image artifacts caused by sound-speed discrepancies. We use this image as a standard in image comparison.

Figure 6 is a comparison of differences between different reconstructed reflectivity images with Fig. 5. The sound-speed model used in (a) and (c) is that in Fig. 3(a), and that used in (b) and (d) is the one shown in Fig. 3(b). Comparisons of Fig. 6(b) with Fig. 6(a), and Fig. 6(d) with Fig. 6(c), show that reflectivity image artifacts decrease with increasing accuracy of the tomography sound-speed results. When the sound-speed discrepancy is large,

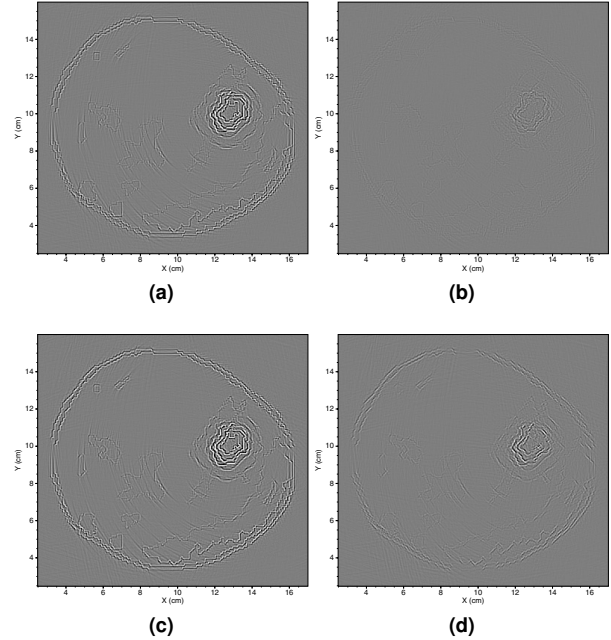


Figure 6: Comparison of the differences (“image artifacts”) of reconstructed reflectivity images compared with the image shown in Fig. 5. Panels (a) and (b) are the differences between the images in Figs. 4(a) and (b) with that in Fig. 5, all obtained using the optimized propagator. Panels (c) and (d) are the corresponding differences of images obtained using the split-step Fourier propagator.

comparison of Fig. 6(a) and Fig. 6(b) indicates that reflectivity images are similar to one another no matter which propagator is used for image reconstruction. That is, image artifacts caused by the sound-speed discrepancy are much stronger than those caused by the propagator inaccuracy when the sound-speed discrepancy is large. When the sound-speed discrepancy is small, comparison of Fig. 6(b) and Fig. 6(d) shows that image artifacts decrease with increasing the propagator accuracy.

Relative image differences in Fig. 7 give a quantitative comparison of image artifacts. We can see that most significant image artifacts occur around the tumor region. The difference between Fig. 7(a) and Fig. 7(c) is insignificant. The image artifacts in Fig. 7(e) are caused by inaccuracy of the split-step Fourier propagator.

4. Conclusions

We have developed an optimized propagator for ultrasound reflectivity imaging and validated it using ultrasound pulse-echo data for a numerical breast phantom. The prop-

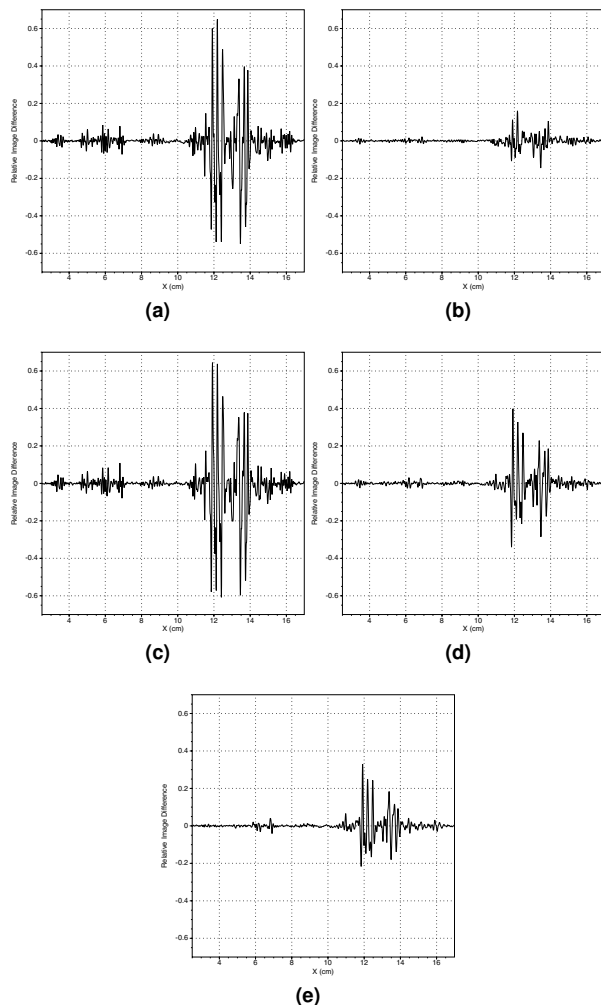


Figure 7: Panels (a)-(d) are respectively the relative image differences along the cross sections of the panels in Fig. 6 at $y=98$ mm. Panel (e) is that for an image obtained using the split-step Fourier propagator and the correct sound speed of the phantom, compared with the image in Fig. 5.

agator is optimized for the sound-speed perturbation range within the breast. Our optimized method is much more accurate than the split-split Fourier method for handling ultrasound scattering in the heterogeneous breast. We have numerically demonstrated the importance of obtaining an accurate sound-speed model of the breast for reflectivity image reconstruction. Our method can produce high-resolution and high-quality ultrasound reflectivity images using an accurate, heterogeneous sound-speed tomography model for image reconstruction.

5. Acknowledgment

This work was supported through the U.S. DOE Laboratory-Directed Research and Development program at Los Alamos National Laboratory.

References

- [1] N. Duric, P. Littrup, L. Poulo, A. Babkin, R. Pevzner, E. Holsapple, and O. Rama. Detection of breast cancer with ultrasound tomography: First results with the computerized ultrasound risk evaluation (cure) prototype. *Med. Phys.*, 34:773–785, 2007.
- [2] N. Duric, P. J. Littrup, A. Babkin, D. Chambers, S. Azevedo, A. Kalinin, R. Pevzner, M. Tokarev, E. Holsapple, O. Rama, and R. Duncan. Development of ultrasound tomography for breast imaging: Technical assessment. *Med. Phys.*, 32:1375–1386, 2005.
- [3] L. Huang, N. Duric, and P. Littrup. Breast imaging with time-reversed ultrasound. In S. Emelianov and W. F. Walker, editors, *Proc. SPIE: Ultrasonic Imaging and Signal Processing*, volume 6147, pages 156–167, Bellingham, Washington, 2006. SPIE.
- [4] L. Huang and Y. Quan. Ultrasound pulse-echo imaging using the split-step fourier propagator. In S. Y. Emelianov and S. A. McAleavey, editors, *Proc. SPIE: Ultrasonic Imaging and Signal Processing*, volume 6513, Bellingham, Washington, 2007. SPIE.
- [5] R. R. Leach Jr., S. G. Azevedo, J. G. Berryman, H. R. Bertete-Aguirre, S. H. Chambers, J. E. Mast, P. Littrup, N. Duric, S. A. Johnson, and F. Wuebbeling. Comparison of ultrasound tomography methods in circular geometry. In M. Insana and W. F. Walker, editors, *Proc. SPIE: Ultrasonic Imaging and Signal Processing*, volume 4687, pages 362–377, Bellingham, Washington, 2002. SPIE.
- [6] S. J. Norton and M. Linzer. Ultrasonic reflectivity tomography: reconstruction with circular transducer arrays. *Ultrasonic Imaging*, 2:154–184, 1979.
- [7] R. G. Pratt, L. Huang, N. Duric, and P. Littrup. Sound-speed and attenuation of the breast tissue using waveform tomography of transmission ultrasound data. In J. Hsieh and M. J. Flynn, editors, *Proc. SPIE: Physics of Medical Imaging*, volume 6510, Bellingham, Washington, 2007. SPIE.
- [8] Y. Quan and L. Huang. Sound-speed tomography using first-arrival transmission ultrasound for a ring array. In S. Y. Emelianov and S. A. McAleavey, editors, *Proc. SPIE: Ultrasonic Imaging and Signal Processing*, volume 6513, Bellingham, Washington, 2007. SPIE.
- [9] E. A. Sickles. Breast imaging: From 1965 to the present. *Radiology*, 215:1–16, 2000.
- [10] R. C. Waag and R. J. Fedewa. A ring transducer system for medical ultrasound research. *IEEE Trans. Ultrason. Ferroelectr. Freq. Control*, 53:1707–1718, 2006.